scientific reports

Check for updates

OPEN

Influence of Kerr nonlinearities on THz radiation generation in air by bichromatic femtosecond laser pulses

Viktorija Tamulienė✉, Urtė Žąsinaitė & Virgilijus Vaičaitis

The dependence of terahertz (THz) radiation generation in air by femtosecond laser pulses on frequency and the relative phase between two-color pump waves was analyzed experimentally and numerically. It was found that although the laser-induced plasma microcurrents remains the main mechanism of THz radiation generation within the whole spectral range, the four-wave mixing modifies the generation process. This modification makes maximal generation efficiency dependent not only on the relative phase between the pump waves but also on the frequency of the emitted radiation. This should be taken into account during the optimization of the generation process in specific spectral ranges.

The advent of powerful femtosecond lasers has enabled the extensive study of various nonlinear optical processes occurring in ambient air over the past few decades. These include air ionization[1,2], third harmonic generation[3,4], four- and six-wave mixing[5–8], supercontinuum generation[9–11], spatial and temporal transformations, and filamentation of propagating laser pulses[12–14], among others. Though these phenomena have applications in atmospheric analysis, spectroscopy, and laser pulse compression[7,9,15–17], the most widely investigated process remains the generation of terahertz radiation by femtosecond bichromatic laser pulses when the fundamental (FH) and second harmonic (SH) beams are focused in air or other gases[18–21]. This method allows for the generation of extremely broadband THz pulses (up to 200 THz[22]) with a high electric field (over 100 MV/cm[23]), making it widely used for various applications, including spectroscopy[24,25], remote sensing, and material characterization[26–29]. However, despite its simplicity from an experimental point of view, the theoretical interpretation of terahertz (THz) radiation generation from laser-created gas plasma has been debated since its discovery. Thus, the first report on THz radiation generation interpreted it as a result of four-wave rectification[30], but an alternative model of plasma-induced microcurrents was soon proposed[31]. It is worth noting that initially, both models predicted similar parameters for the generated THz radiation, such as pulse energy dependence on pump power, spectral width, polarization, etc. The main difference was the relative phase value θ between the bichromatic pump components when the THz generation yield was predicted to be maximal (optimal phase difference θ_0). Specifically, the four-wave rectification model found the θ_0 to be 0, whereas the plasma microcurrent model predicted θ_0 to be $\pi/2$[18,31–34]. However, since it is impossible to directly measure θ within the interaction area, many papers have been published in favor of one model or another (see for example[35–39] and references therein). Nevertheless, the theory of plasma microcurrents gradually became the primary basis for the theoretical and numerical interpretation of experimental results (see references[40–42]). On the other hand, a few papers have been published that suggest the joint action of Kerr nonlinearities and plasma microcurrents in THz radiation generation[43–45]. It was predicted that the spectral ranges of THz emission caused by these two phenomena would differ, which could be used to distinguish between the two processes. However, the spectra caused by these phenomena overlap to a great extent. Moreover, it was shown that Kerr-based THz emission is usually much weaker than plasma microcurrent-based THz emission within the whole spectral range of generated radiation[44], which makes it practically impossible to identify which phenomenon is responsible for generating a specific THz frequency based solely on the spectra of the generated THz emission. Therefore, this paper reports a proof-of-principle experiment demonstrating that the phase dependence of THz emission is also a function of the frequency of the generated radiation. This finding indicates an interplay between Kerr nonlinearity and plasma-based effects on the THz radiation generation process that should be considered when developing relevant theoretical models.

Laser Research Center, Vilnius University, Saulėtekio 10, Vilnius 10223, Lithuania. ✉email: viktorija.tamuliene@ff.vu.lt

Results

Experimental results

As expected, the power of the generated THz radiation depended strongly on the pump power and the position of the nonlinear beta barium borate (BBO) crystal (i.e., its distance from the plasma spot), which was directly related to the relative phase difference θ between the FH and SH waves[31,46]. Thus, when the crystal was moved along the pump beam, the THz power oscillated with a period of approximately 2.5 cm (Fig. 1a). However, note that the phase of the oscillations clearly depended on the pump power. This could be the result of varying plasma influence on the relative delay between the FH and SH pulses at the point of THz radiation generation[47]. Additionally, in contrast to most similar experiments using electro-optical sampling (EOS)[31,33,48,49], the THz signal never decreased to zero for any laser power or crystal coordinate. Furthermore, the modulation depth (MD), defined as the ratio of the one half of the peak-to-peak change to the mean value, was quite low (30-35%). This result can be explained by the fact that EOS is an inherently bandwidth-limited technique[50]. In our experiment, we used a broadband THz detector that is sensitive in the range of 0.1–300 THz, thus covering the entire spectrum of generated THz radiation (Fig. 2b). More specifically, to explain this result, we assumed that the dependence of THz power on θ was a function of frequency. Therefore, we repeated the measurements using spectrally narrowed THz emission. To select specific spectral ranges, we placed wavelength-selective materials (WSMs), including Teflon, germanium (Ge), sapphire, and a commercially available long-pass THz filter (LPF23.4-35, Tydex Company), in front of the detector or spectrometer (Fig. 6) during the measurements. The spectra of THz radiation transmitted through the WSMs are shown in Fig. 2.

Thus, while the initially generated THz radiation had a spectral width of over 50 THz (Fig. 1b), the spectral ranges selected after transmission through the WSMs were significantly narrower (from a few to a few tens of THz, depending on the material and spectral range). Table 1 summarizes the specific thicknesses of the WSMs and the corresponding spectral characteristics of the transmitted THz radiation.

Figure 3 shows the typical power dependence of THz radiation transmitted through WSMs on the BBO crystal coordinate. As with the full THz power (Fig. 1a), the power of spectrally narrowed radiation oscillated with the same period of about 2.5 cm. However, the phase of these oscillations depended clearly on the wavelength-selecting materials used, i.e., on the frequency of the tested radiation. Thus, compared to the dependence obtained for the full spectrum of generated radiation, inserting the Ge wafer or Tydex filter shifts the corresponding curves to the left by approximately 1.7 and 3.3 mm, respectively (Fig. 3a). These shifts correspond to shorter optical beam paths in air between the nonlinear crystal and plasma, and consequently, to a smaller phase difference θ between the FH and SH waves within the generation region, see Discussion Section for the relation between the optical path and phase shift. Qualitative analysis of the data revealed a clear dependence: θ increases with the frequency of the generated radiation. Thus, the curve obtained using the sapphire wafer, which transmits radiation with frequencies over 50 THz, shifted the most to the right (green curve in Fig. 3b). Meanwhile, the radiation with lower central frequencies (20 and 11 THz, selected by the Ge and Teflon filters, respectively) demonstrated corresponding phase decreases (blue and magenta curves in Fig. 3b, respectively). Furthermore, compared to the full THz power, the modulation depth of the radiation filtered by Teflon significantly increased (from 30-35% to over 80%; compare Fig. 1a with the magenta curve in Fig. 3b), though the total registered power of the radiation decreased significantly. However, this increase in modulation depth was observed only in the case of Teflon and can tentatively be explained by the fact that it transmitted radiation with the narrowest spectral width (a few THz, Fig. 2a).

Note that inserting the WSMs into the THz beam path after the plasma spot cannot affect the generation conditions, i.e., the dependence of the THz yield on θ for any wavelength of emission. However, we observed a similar increase in θ with laser power. This increase is apparently caused by an increase in plasma density and volume, which affects the phases of both pump waves[47]. However, the introduction of WSMs into the THz beam path results in frequency and phase modulation, but in a linear propagation conditions (which was the case in

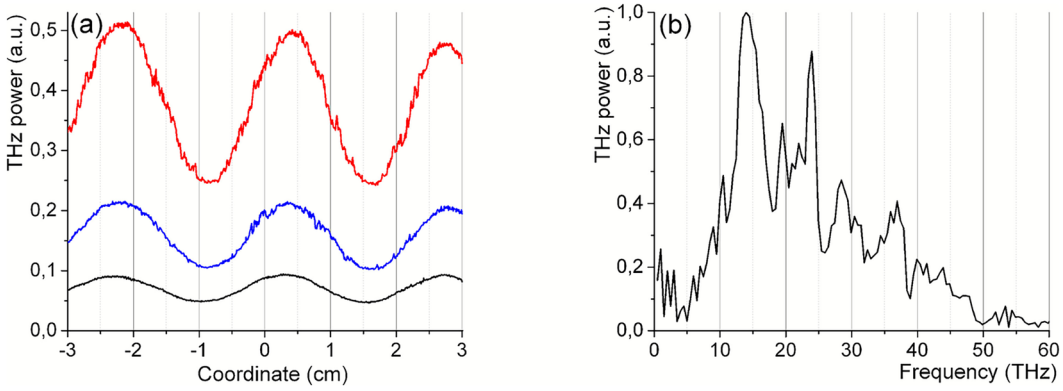

Figure 1. (**a**) THz power as a function of the BBO crystal coordinate for laser pulse energies of 0.1, 0.12, and 0.16 mJ. Positive coordinate values correspond to a longer optical beam path between the nonlinear crystal and the plasma (the FH pulse comes first). (**b**) A typical spectrum of THz radiation generated in air plasma.

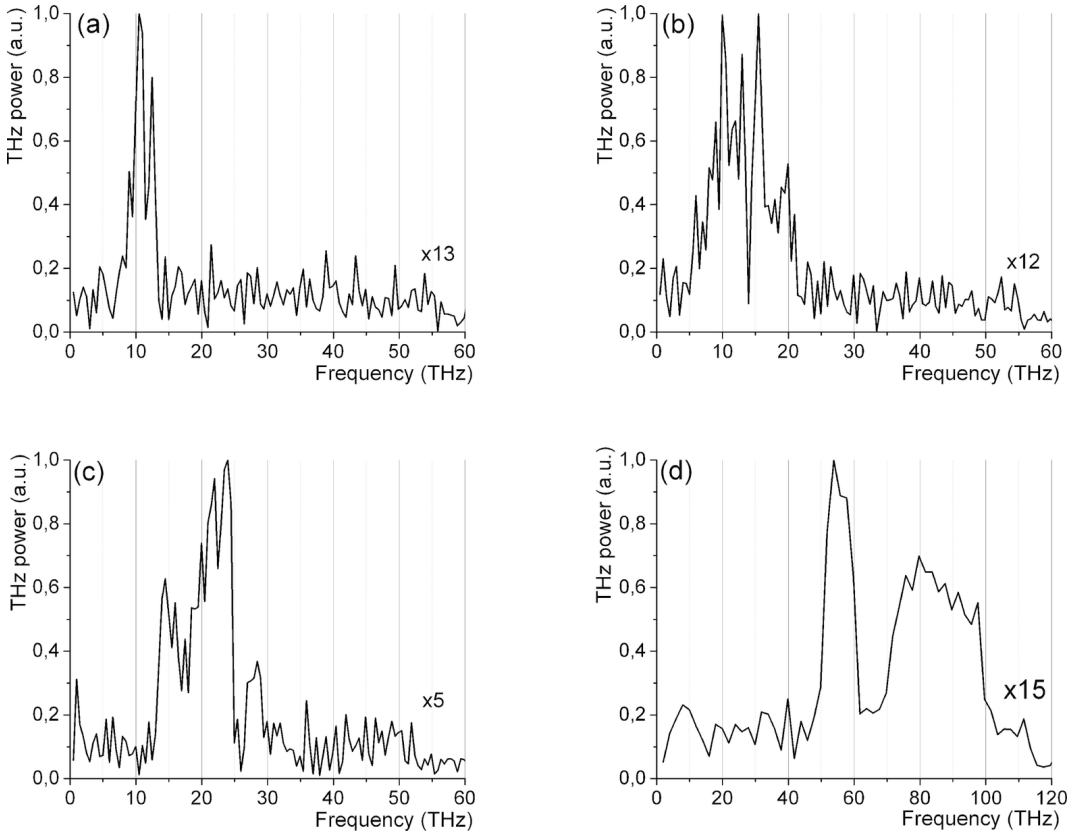

Figure 2. Spectra of THz radiation generated in the air plasma and transmitted through (**a**) the 1 mm-thick Teflon wafer, (**b**) the long-pass filter (Tydex, LPF23.4-35), (**c**) the 2 mm-thick Ge and (**d**) the 2 mm-thick Sapphire wafer. Scaling factors represent the ratio of specific spectral intensity with that obtained without any wavelength selecting materials (Fig. 1b).

Material (thickness)	Teflon (1 mm)	Tydex filter	Ge (2 mm)	Sapphire (2 mm)
Frequency (width)	11 (3.5) THz	13 (8.5) THz	20 (11) THz	75 (40) THz

Table 1. Used WSMs and their thicknesses with corresponding approximate central frequencies and spectral widths of transmitted THz radiation.

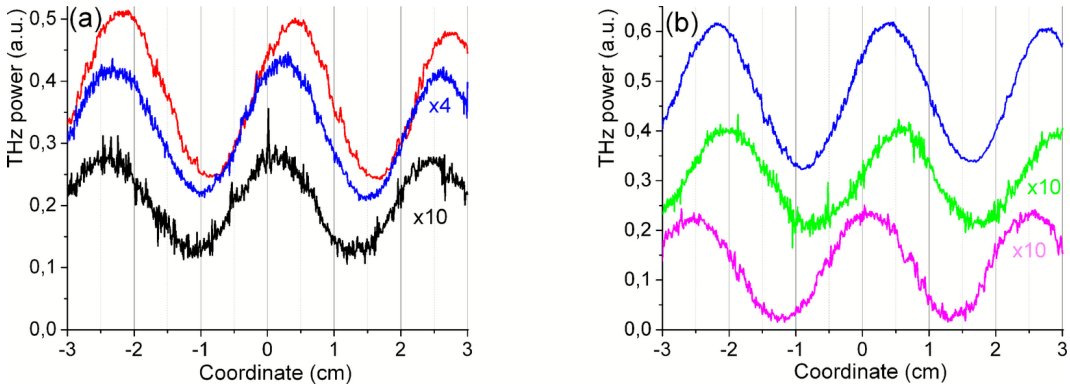

Figure 3. THz beam power dependence on the BBO crystal coordinate: (**a**) measured directly (red line) and transmitted through Ge and Tydex filters (blue and black curves, respectively) for laser pulse energies of 0.16 mJ. (**b**) Transmitted through Ge, sapphire, and Teflon (blue, green, and magenta lines, respectively) for laser pulse energies of 0.3 mJ.

our experiment) these effects did not influence the measured phase dependencies (for example, shown in Fig. 3, etc.).

Numerical results

The results of the numerical modeling essentially confirmed the primary experimental findings. Thus, Fig. 4a shows that the power of the generated THz radiation oscillates as the relative phase between the FH and SH waves varies. Furthermore, this figure demonstrates that the phase of these oscillations is a function of a frequency. To further understand this phenomenon, we analyzed in more detail how the output optimal phase difference θ_0 depends on frequency and propagation distance (coordinate z). Note however, that phase θ is defined as the input parameter (see Eq. 4). We evaluated the optimal phase difference θ_0 from the corresponding θ-dependencies at different propagation lengths (z values). The results are presented in Figs. 4b and 5a. As one can see, at the onset of the plasma generation stage ($z/f = 0.89$), the optimal phase difference θ_0 is almost frequency independent. On the other hand, at the output ($z/f > 1$) θ_0 is frequency-dependent, as it was observed in the experiment. With the change of the propagation distance, the optimal phase varies by different law for different frequency components (Fig. 5a). The most prominent phase change is obtained just before the vicinity of the lens focus where the plasma density reaches its maximum (Fig. 5b). Note that the plasma density is dependent on the input phase values, see blue and red lines for $\theta = 0$ and $\theta = \pi/2$, respectively, in Fig. 5b. This observation can be explained by different sum field shapes of the bichromatic pump pulses. In addition, we performed the numerical simulation without the Kerr term. The phase jump of around $\pi/2$ which is obtained at the vicinity of the focus in both cases (Fig. 5a, all terms included and Fig. 5c, Kerr term excluded) can be explained by the transition to the intense plasma generation mechanism. At the output, the value θ_0 is different for these two cases, therefore we conclude that the nonlinear Kerr effect influences the optimal phase difference.

Discussion

The numerical simulation results confirm the experimental findings. Both in the experiment (Fig. 3a,b) and theory (Fig. 4a) we observe the oscillations in THz output signal initiated by the change of the input phase difference of fundamental and second harmonics waves. Note, that in the experiment, by shifting the nonlinear crystal by distance z_1, the relative phase changes by the amount of $|\Delta k|z_1$, where $\Delta k = 2k_{10} - k_{20}$ and k_{10}, k_{20} are the wavenumbers of FH (index 1) and SH (index 2) waves, respectively. The curves in Fig. 4a are π-periodic. This period corresponds to distance $z_1 = \pi/|\Delta k| = 2.6$ cm which is in good qualitative agreement with the experimental measurements (about 2.5 cm). As it was noted, the output optimal phase for THz generation is frequency dependent. For instance, the estimated numerical phase shift between 20 THz and 10 THz is 0.05π, while the experimental shifts for Ge wafer and Tydex filter were 1.7 mm and 3.3 mm, respectively, and their difference 1.6 mm corresponds to 0.06π. In the numerical simulations, the optimal phase θ_0 monotonically increases in the range from 4 THz to 30 THz, and in the remaining range from 30 THz to 60 THz it decreases (Fig. 4b). In the experiment, only the increase of θ was observed since the spectrum width of Sapphire WSM was large and the lower frequencies play the major role for the output THz power. Note that the direct measurements of the THz spectra at different relative phases would be more intuitive and should give the same result. However, due to the comparably large fluctuations of the spectral intensity obtained using the interferometric method, we were not able to record directly the reliable phase dependencies as a function of THz radiation frequency.

It is worth to mention that the alternative explanation of our results is possible in the case if the frequency of generated THz emission was a function of coordinate along the optical axis. Then to compensate for the plasma-induced phase shifts, the second harmonic crystal should have to be moved away from the plasma, while its final position was frequency dependent. Though at the moment to the best of our knowledge we are not aware

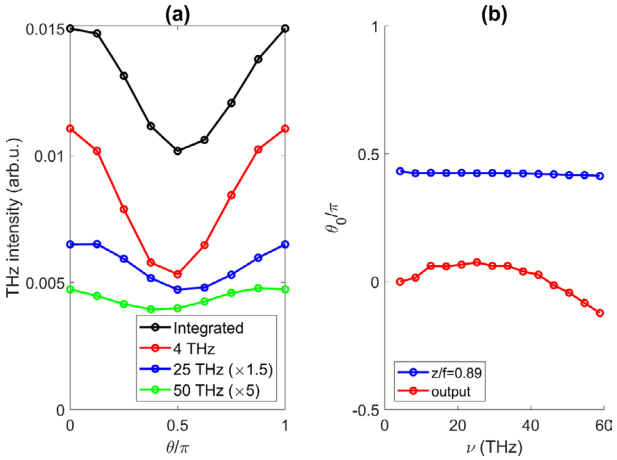

Figure 4. Numerical calculations. (**a**) Dependence of the output THz spectral intensity on frequency and the relative phase θ between the FH and SH waves, integrated within the entire spectrum of generated emissions and within 4 THz ranges centered at 4, 25 and 50 THz. (**b**) Dependence of the optimal phase difference between the FH and SH waves on frequency at $z/f = 0.89$ (blue line) and after the plasma spot (red line).

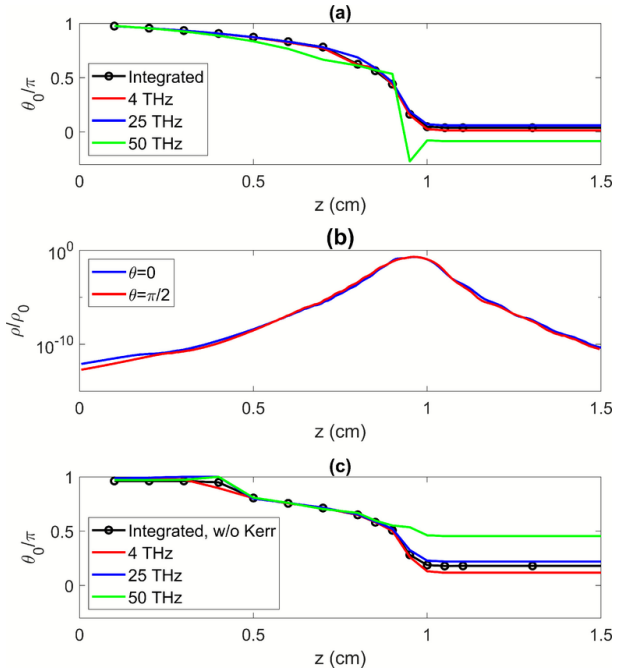

Figure 5. Numerical calculations. (**a**) Dependence of optimal phase difference on propagation distance for integrated THz spectrum as well as three different frequencies: 4 THz, 25 THz and 50 THz. (**b**) Dependence of plasma density on propagation distance at input phase difference 0 and $\pi/2$. (**c**) Dependence of optimal phase difference on propagation distance for integrated THz spectrum as well as three different frequencies: 4 THz, 25 THz and 50 THz when Kerr term was omitted in Eq. (1). In the simulations, focus length $f = 1$ cm.

of any simultaneously coordinate and frequency dependent THz emissions, this alternative model can not be rulled out completely, because many plasma and light intensity dependent phenomena, specifically not analyzed in our model, such as plasma defocusing or Kerr self-focusing, etc., are frequency and intensity dependent and, as the light intensity and plasma density varies along the optical axis, could lead to generation of radiations with the frequencies dependent on the coordinate. In conclusion, we have demonstrated both experimentally and numerically, that during terahertz radiation generation in air by focused two-color femtosecond laser pulses the optimal phase between the two pump waves is a function of frequency of generated THz radiation. This phenomenon is believed to result from the interplay of two nonlinear sources of terahertz emission: the four-wave mixing and the laser-induced plasma photocurrents. Although the former was estimated to be much weaker than the latter, FWM can still modify the phase relations between the interacting waves during propagation via self- and cross-phase modulation, self-steepening, and other nonlinear processes[51]. Therefore, apart from estimating the relative contributions of various nonlinear phenomena to THz radiation generation, our findings could help test or validate theoretical models of ultrafast ionization, as well as nonlinear propagation and filamentation of femtosecond laser pulses in gaseous media. Our research results should also be considered when implementing broadband or tunable gas-based THz radiation sources, since the relative phase between the pump waves must be optimized for each specific THz radiation spectral range.

Methods

Experimental methods

Figure 6 shows the experimental setup used for THz radiation generation and characterization. A Ti:Sapphire femtosecond laser ($\lambda = 790$ nm, τ (at full width half maximum (FWHM)) = 35–40 fs, 1 kHz repetition rate) was used as the pump source. First, the fundamental laser beam (FH) passed through a nonlinear BBO crystal (100 μm thick), which generated a second harmonic (SH) at a wavelength of approximately 395 nm. Next, two elements were introduced to enhance the efficiency of terahertz radiation generation: a double-wavelength wave plate to align the polarizations of the FH and SH waves, and a group velocity delay compensator to coarsely adjust the delay (relative phase θ) between these waves. Fine-tuning of the phase was achieved by moving the BBO crystal along the optical axis. The optimal orientations of the wave plate and compensator were determined experimentally by rotating them and observing the THz signal. With the help of a flat dichroic dielectric mirror, the bichromatic laser beam was then redirected toward a spherical concave mirror with a focal length of 100 mm, which focused the beam into a tiny spot. This produced a plasma spot where THz radiation was generated. A THz filter (a 0.5–1 mm thick silicon wafer) was placed behind the plasma filament to remove visible and near-infrared pump radiation from the THz beam. A parabolic mirror with an effective focal length (EFL) of 152.4 mm was used to collimate the THz beam since, under the given experimental conditions, the THz radiation is emitted in the form of a hollow cone with an apex angle of a few degrees[46,52–54]. The two other parabolic mirrors (EFLs 381 and 101.6 mm) formed a telescope that reduced the diameter of the THz beam. The beam was

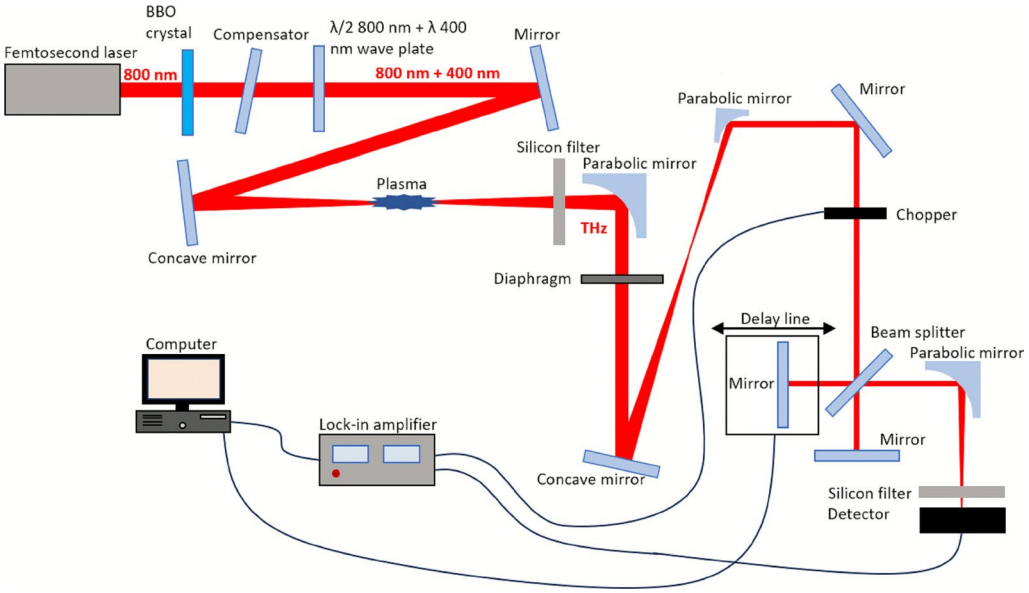

Figure 6. Experimental setup used for THz radiation generation and characterization, when phase difference between the FH and SH waves was controlled by translating the nonlinear SH crystal.

then directed into a homemade Michelson interferometer for spectral analysis by the flat, metal-coated mirror. THz radiation power could be directly measured with a calibrated, removable THz detector (TPR-A-65 THz, Spectrum Detector Inc.) placed in the THz beam's path before the spectrometer. To increase the sensitivity and signal-to-noise ratio of the power and spectral measurements, the beam was modulated by a mechanical beam chopper (modulation rate: 5 Hz) synchronized with a computer-controlled lock-in amplifier. Note that to select specific spectral parts of the generated THz emission we used additional materials (e.g., fused silica, sapphire, Teflon) placed in front of the detector or interferometer (not shown in Fig. 6).

Numerical methods

For the numerical analysis we have simulated the unidirectional pulse propagation equation (UPPE). Thus, for the the Fourier transform $\widehat{\mathscr{E}}(\omega, k_\perp, z)$ of the analytic signal $\mathscr{E}(t, r, z)$ we write

$$\frac{\partial \widehat{\mathscr{E}}}{\partial z} = iK'_z\widehat{\mathscr{E}} + i\widehat{P}_{\text{Kerr}} - i\widehat{P}_{\text{pl}} - \widehat{P}_{\text{loss}}. \tag{1}$$

The simulations were performed in the cylindrical coordinates (*r*,*z*) with azimuth symmetry, where $r = \sqrt{x^2 + y^2}$ and (*x*, *y*, *z*) are the Cartesian coordinates. *t* is the retarded time in the fundamental wave (FW) co-moving frame, $i = \sqrt{-1}$. The real field is given by $E(t, r, z) = \text{Re}\,(\mathscr{E}(t, r, z))$. The first rhs. term describes linear propagation – beam diffraction and pulse walk-off as well as dispersion. $K'_z = K_z - \omega/u_0$, where $K_z = \sqrt{k^2(\omega) - k_\perp^2}$ is the longitudinal wavevector component, $k(\omega) = \frac{2\pi}{\lambda}n(\lambda)$ is the wavenumber, $\omega = \frac{2\pi c}{\lambda}$ is the angular frequency, λ is the wavelength and c is speed of light. $n(\lambda)$ is the wavelength-dependent refractive index of air found from the Sellmeier equation[55]. u_0 is the group velocity at FW frequency. $\widehat{P}_{\text{Kerr}} = \frac{4}{3n}n_2\varepsilon_0\omega\text{FT}\left(E^3(t, r, z)\right)$ describes the nonlinear interaction in the medium. $\text{FT}(\circ)$ is the Fourier transform operation. n_2 is the nonlinear refractive index, ε_0 is the vacuum permittivity. The two last rhs. terms are associated with the air plasma. The first one, $\widehat{P}_{pl} = \frac{e^2}{2m_e c\varepsilon_0 n}\frac{1}{\omega + i\nu_c}\text{FT}[\rho\mathscr{E}]$, where *e* and m_e are the electron charge and mass, respectively. ν_c is the collision frequency and ρ is the plasma density. The last was calculated from the differential equation:

$$\frac{\partial \rho_{O,N}}{\partial t} = (m_{O,N}\rho_0 - \rho_{O,N})W_{O,N}(t), \tag{2}$$

where ρ_0 is the number density of air and $W_{O,N}$ defines the ionization rate of either oxygen or nitrogen molecules – the main constituents of air. Fraction $m_O = 0.2$ and $m_N = 0.8$. The total density $\rho = \rho_O + \rho_N$. The ionization rate *W*(*t*) was calculated by the use of the Perelomov, Popov, and Terent'ev (PPT) model[56] adopting Ref.[57] charge numbers $Z^*_{O_2} = 0.53$ for dioxygen and $Z^*_{N_2} = 0.9$ for di-nitorgen. The nonlinear loss term is given by: In this case, the nonlinear losses are given by

$$\widehat{P}_{\text{loss}} = \text{FT}\left(\left[W_O U_O(m_O\rho_0 - \rho_O) + W_N U_N(m_N\rho_0 - \rho_N)\right]\frac{1}{\text{Re}(\mathscr{E})2\varepsilon_0 c}\right). \tag{3}$$

Parameter	Notation	Value
FW wavelength	λ_{10}	800 nm
SH wavelength	λ_{20}	400 nm
FW energy	E_{10}	100 μJ
SH energy	E_{20}	10 μJ
Pulse duration (FWHM)	τ	35 fs
FW beam diameter	$2r_{10}$	0.5 mm
SH beam diameter	$2r_{20}$	$\frac{0.5}{\sqrt{2}}$ mm
focal length	f	1 cm

Table 2. Input parameters.

Coefficient	Value
ρ_0	2.7×10^{25} m^{-3}
n_2	10^{-23} m^2/W
ν_c	2.85 ps^{-1}

Table 3. Simulation coefficients.

At the input, $z = 0$, the field is described by the sum of FW (index 1) and second harmonic (SH, index 2) waves:

$$\mathscr{E}(t, r, z = 0) = \mathscr{E}_{10}(t, r) + \mathscr{E}_{20}(t, r) \exp(i\theta), \tag{4}$$

where θ is the phase difference. Each of the fields is given by

$$\begin{aligned} &\mathscr{E}_{j0}(t, r) = a_{j0} \\ &\times \mathrm{IFT}_\mathrm{t} \left(\mathrm{FT}_\mathrm{t} \left[\exp(-i\omega_{j0} t) \exp\left(-2\ln(2) \tfrac{t^2}{\tau^2} \right) \right] \exp\left(-i \tfrac{\omega r^2}{2fc} - \tfrac{r^2}{r_{j0}^2} \right) \right). \end{aligned} \tag{5}$$

where $j = 1, 2$. $\mathrm{FT}_t(\circ)$ and $\mathrm{IFT}_t(\circ)$ are the Fourier transform and inverse Fourier transform in time domain. ω_{j0} is the central angular frequency, τ is the pulse duration at FWHM and r_{j0} is the beam radius at $1/e^2$ level. f is the focal length of the lens and a_{j0} is the input amplitude. The input parameters are presented in Table 2 while the simulation coefficients are given in Table 3.

Equation (1) was simulated by the use of the Fourier split-step method[58]. Due to the azimuth symmetry, fast Hankel transform was utilized[59]. The time window $[-4\tau,\ 4\tau)/\sqrt{2\ln(2)}$ was divided into 2024 equal steps. The radial coordinate $r \in (0,\ 2r_0)$ had 300 steps. The longitudinal step was adopted at each propagation distance with respect to the maximum pump intensity as well as plasma density.

Data availability

The datasets used and/or analyzed in this study are accessible from the corresponding author upon reasonable request.

Received: 10 October 2025; Accepted: 23 December 2025
Published online: 06 January 2026

References

1. Théberge, F., Liu, W., Simard, P. T., Becker, A. & Chin, S. L. Plasma density inside a femtosecond laser filament in air: Strong dependence on external focusing. *Phys. Rev. E* **74**, 036406. https://doi.org/10.1103/PhysRevE.74.036406 (2006).
2. Xu, H., Cheng, Y., Chin, S.-L. & Sun, H.-B. Femtosecond laser ionization and fragmentation of molecules for environmental sensing. *Laser Photon. Rev.* **9**, 275–293. https://doi.org/10.1002/lpor.201400208 (2015).
3. Aközbek, N. et al. Third-harmonic generation and self-channeling in air using high-power femtosecond laser pulses. *Phys. Rev. Lett.* **89**, 143901. https://doi.org/10.1103/PhysRevLett.89.143901 (2002).
4. Liu, Y. et al. Efficient generation of third harmonic radiation in air filaments: A revisit. *Opt. Commun.* **284**, 4706–4713. https://doi.org/10.1016/j.optcom.2011.05.050 (2011).
5. Vaičaitis, V. Cherenkov-type phase-matched third harmonic generation in air. *Opt. Commun.* **185**, 197–202. https://doi.org/10.1016/S0030-4018(00)00997-4 (2000).
6. Théberge, F., Aközbek, N., Liu, W., Becker, A. & Chin, S. L. Tunable ultrashort laser pulses generated through filamentation in gases. *Phys. Rev. Lett.* **97**, 023904. https://doi.org/10.1103/PhysRevLett.97.023904 (2006).
7. Karashima, S., Chen, C.-J. & Suzuki, T. Generation of sub-10-fs deep and extreme ultraviolet pulses for time-resolved photoemission spectroscopy. *Opt. Lett.* **49**, 3777–3780. https://doi.org/10.1364/OL.528323 (2024).
8. Vaičaitis, V., Jarutis, V., Steponkevičius, K. & Stabinis, A. Noncollinear six-wave mixing of femtosecond laser pulses in air. *Phys. Rev. A* **87**, 063825. https://doi.org/10.1103/PhysRevA.87.063825 (2013).

9. Kasparian, J. & Wolf, J.-P. Physics and applications of atmospheric nonlinear optics and filamentation. *Opt. Express* **16**, 466–493. https://doi.org/10.1364/OE.16.000466 (2008).
10. Vaičaitis, V., Butkus, R., Balachninaitė, O., Morgner, U. & Babushkin, I. Diffraction-enhanced femtosecond white-light filaments in air. *Appl. Phys. B* **124**, 221. https://doi.org/10.1007/s00340-018-7090-y (2018).
11. Liu, Y. et al. Stable, intense supercontinuum light generation at 1 kHz by electric field assisted femtosecond laser filamentation in air. *Light Sci. Appl.* **13**, 42. https://doi.org/10.1038/s41377-023-01364-3 (2024).
12. Couairon, A. & Mysyrowicz, A. Femtosecond filamentation in transparent media. *Phys. Rep.* **441**, 47–189. https://doi.org/10.1016/j.physrep.2006.12.005 (2007).
13. Koritsoglou, O., Loison, D., Uteza, O. & Mouskeftaras, A. Characteristics of femtosecond laser-induced shockwaves in air. *Opt. Express* **30**, 37407–37415. https://doi.org/10.1364/OE.468224 (2022).
14. Ran, Q., Li, H., Chang, W. & Wang, Q. Self-compression of high energy ultrashort laser pulses. *Laser Photon. Rev.* **18**, 2300595. https://doi.org/10.1002/lpor.202300595 (2024).
15. Xu, H., Cheng, Y., Chin, S.-L. & Sun, H.-B. Femtosecond laser ionization and fragmentation of molecules for environmental sensing. *Laser Photon. Rev.* **9**, 275–293. https://doi.org/10.1002/lpor.201400208 (2015).
16. Zhang, Z. et al. Detection of 1.4 $\mu g/m^3$ Na^+ in aerosol at a 30 m distance using 1 kHz femtosecond laser filamentation in air. *Opt. Express* **31**, 6464–6474. https://doi.org/10.1364/OE.481577 (2023).
17. Mei, H. et al. Fluorescence and lasing of neutral nitrogen molecules inside femtosecond laser filaments in air: mechanism and applications. *Phys. Chem. Chem. Phys.* **26**, 23528–23543. https://doi.org/10.1039/D4CP01626B (2024).
18. Roskos, H., Thomson, M., Kreß, M. & Löffler, T. Broadband THz emission from gas plasmas induced by femtosecond optical pulses: From fundamentals to applications. *Laser Photon. Rev.***1**, 349–368. https://doi.org/10.1002/lpor.200710025.
19. Sun, W., Wang, X. & Zhang, Y. Terahertz generation from laser-induced plasma. *Opto-Electron. Sci.* **1**, 220003–1–220003–27. https://doi.org/10.29026/oes.2022.220003 (2022).
20. Buožius, D. et al. Terahertz and far infrared radiation generation in air plasma created by bichromatic subpicosecond laser pulses. *Appl. Phys. Lett.* **124**, 071113. https://doi.org/10.1063/5.0188581 (2024).
21. Alirezaee, H. et al. Universal properties of locally generated terahertz waveforms from polarization-controlled two- and multicolor ionizing fields. *Phys. Rev. Res.* **7**, 033057. https://doi.org/10.1103/dj4k-q4x2 (2025).
22. Matsubara, E., Nagai, M. & Ashida, M. Ultrabroadband coherent electric field from far infrared to 200 THz using air plasma induced by 10 fs pulses. *Appl. Phys. Lett.* **101**, 011105. https://doi.org/10.1063/1.4732524 (2012).
23. Koulouklidis, A. D. et al. Observation of extremely efficient terahertz generation from mid-infrared two-color laser filaments. *Nat. Commun.* **11**, 292. https://doi.org/10.1038/s41467-019-14206-x (2020).
24. D'Angelo, F., Mics, Z., Bonn, M. & Turchinovich, D. Ultra-broadband THz time-domain spectroscopy of common polymers using THz air photonics. *Opt. Express* **22**, 12475–12485. https://doi.org/10.1364/OE.22.012475 (2014).
25. Paingad, V. C. et al. Ultrafast plasmon thermalization in epitaxial graphene probed by time-resolved THz spectroscopy. *Adv. Func. Mater.* **31**, 2105763. https://doi.org/10.1002/adfm.202105763 (2021).
26. Liu, J., Dai, J., Chin, S. L. & Zhang, X.-C. Broadband terahertz wave remote sensing using coherent manipulation of fluorescence from asymmetrically ionized gases. *Nat. Photonics* **4**, 627–631. https://doi.org/10.1038/nphoton.2010.165 (2010).
27. Talbi, A. et al. Remote terahertz spectroscopy from extended two-color plasma filaments: The altesse 2 project. *Europhys. Lett.* **143**, 10001. https://doi.org/10.1209/0295-5075/acdc4c (2023).
28. Wen, H., Wiczer, M. & Lindenberg, A. M. Ultrafast electron cascades in semiconductors driven by intense femtosecond terahertz pulses. *Phys. Rev. B* **78**, 125203. https://doi.org/10.1103/PhysRevB.78.125203 (2008).
29. Vaičaitis, V., Balachninaitė, O., Matijošius, A., Babushkin, I. & Morgner, U. Direct time-resolved plasma characterization with broadband terahertz light pulses. *Phys. Rev. E* **107**, 015201. https://doi.org/10.1103/PhysRevE.107.015201 (2023).
30. Cook, D. J. & Hochstrasser, R. M. Intense terahertz pulses by four-wave rectification in air. *Opt. Lett.* **25**, 1210–1212. https://doi.org/10.1364/OL.25.001210 (2000).
31. Kim, K. Y., Glownia, J. H., Taylor, A. J. & Rodriguez, G. Terahertz emission from ultrafast ionizing air in symmetry-broken laser fields. *Opt. Express* **15**, 4577–4584. https://doi.org/10.1364/OE.15.004577 (2007).
32. Xie, X., Dai, J. & Zhang, X.-C. Coherent control of THz wave generation in ambient air. *Phys. Rev. Lett.* **96**, 075005. https://doi.org/10.1103/PhysRevLett.96.075005 (2006).
33. Dietze, D. et al. Polarization of terahertz radiation from laser generated plasma filaments. *J. Opt. Soc. Am. B* **26**, 2016–2027. https://doi.org/10.1364/JOSAB.26.002016 (2009).
34. Dai, J., Karpowicz, N. & Zhang, X.-C. Coherent polarization control of terahertz waves generated from two-color laser-induced gas plasma. *Phys. Rev. Lett.* **103**, 023001. https://doi.org/10.1103/PhysRevLett.103.023001 (2009).
35. Houard, A., Liu, Y., Prade, B. & Mysyrowicz, A. Polarization analysis of terahertz radiation generated by four-wave mixing in air. *Opt. Lett.* **33**, 1195–1197. https://doi.org/10.1364/OL.33.001195 (2008).
36. Chen, Y. et al. Elliptically polarized terahertz emission through four-wave mixing in a two-color filament in air. *Opt. Commun.* **282**, 4283–4287. https://doi.org/10.1016/j.optcom.2009.07.044 (2009).
37. Wen, H. & Lindenberg, A. M. Coherent terahertz polarization control through manipulation of electron trajectories. *Phys. Rev. Lett.* **103**, 023902. https://doi.org/10.1103/PhysRevLett.103.023902 (2009).
38. Thomson, M. D., Blank, V. & Roskos, H. G. Terahertz white-light pulses from an air plasma photo-induced by incommensurate two-color optical fields. *Opt. Express* **18**, 23173–23182. https://doi.org/10.1364/OE.18.023173 (2010).
39. Peñano, J., Sprangle, P., Hafizi, B., Gordon, D. & Serafim, P. Terahertz generation in plasmas using two-color laser pulses. *Phys. Rev. E* **81**, 026407. https://doi.org/10.1103/PhysRevE.81.026407 (2010).
40. Zhang, D. et al. Synchronizing terahertz wave generation with attosecond bursts. *Phys. Rev. Lett.* **109**, 243002. https://doi.org/10.1103/PhysRevLett.109.243002 (2012).
41. Bergé, L., Skupin, S., Köhler, C., Babushkin, I. & Herrmann, J. 3D numerical simulations of THz generation by two-color laser filaments. *Phys. Rev. Lett.* **110**, 073901. https://doi.org/10.1103/PhysRevLett.110.073901 (2013).
42. Clerici, M. et al. Wavelength scaling of terahertz generation by gas ionization. *Phys. Rev. Lett.* **110**, 253901. https://doi.org/10.1103/PhysRevLett.110.253901 (2013).
43. Borodin, A. V. et al. Transformation of terahertz spectra emitted from dual-frequency femtosecond pulse interaction in gases. *Opt. Lett.* **38**, 1906–1908. https://doi.org/10.1364/OL.38.001906 (2013).
44. Andreeva, V. A. et al. Ultrabroad terahertz spectrum generation from an air-based filament plasma. *Phys. Rev. Lett.* **116**, 063902. https://doi.org/10.1103/PhysRevLett.116.063902 (2016).
45. Zhao, J. et al. Clue to a thorough understanding of terahertz pulse generation by femtosecond laser filamentation. *Photon. Res.* **6**, 296. https://doi.org/10.1364/PRJ.6.000296 (2018).
46. You, Y. S., Oh, T. I. & Kim, K. Y. Off-axis phase-matched terahertz emission from two-color laser-induced plasma filaments. *Phys. Rev. Lett.* **109**, 183902. https://doi.org/10.1103/PhysRevLett.109.183902 (2012).
47. Tamulienė, V., Buožius, D. & Vaičaitis, V. Plasma-assisted temporal shifts of bichromatic femtosecond laser pulses in air. *Phys. Rev. A* **103**, 033502. https://doi.org/10.1103/PhysRevA.103.033502 (2021).
48. Kress, M., Löffler, T., Eden, S., Thomson, M. & Roskos, H. G. Terahertz-pulse generation by photoionization of air with laser pulses composed of both fundamental and second-harmonic waves. *Opt. Lett.* **29**, 1120–1122. https://doi.org/10.1364/OL.29.001120 (2004).

49. Pyragaitė, V., Smilgevičius, V., Steponkevičius, K., Makauskas, B. & Vaičaitis, V. Phase shifts in terahertz wave generation by tightly focused bichromatic laser pulses. *J. Opt. Soc. Am. B* **31**, 1430–1435. https://doi.org/10.1364/JOSAB.31.001430 (2014).
50. Neu, J. & Schmuttenmaer, C. A. Tutorial: An introduction to terahertz time domain spectroscopy (THz-TDS). *J. Appl. Phys.* **124**, 231101. https://doi.org/10.1063/1.5047659 (2018).
51. Nguyen, A. et al. Spectral dynamics of THz pulses generated by two-color laser filaments in air: the role of kerr nonlinearities and pump wavelength. *Opt. Express* **25**, 4720–4740. https://doi.org/10.1364/OE.25.004720 (2017).
52. Zhong, H., Karpowicz, N. & Zhang, X.-C. Terahertz emission profile from laser-induced air plasma. *Appl. Phys. Lett.* **88**, 261103. https://doi.org/10.1063/1.2216025 (2006).
53. Vaičaitis, V. et al. Influence of laser-preformed plasma on THz wave generation in air by bichromatic laser pulses. *Laser Phys.* **28**, 095402. https://doi.org/10.1088/1555-6611/aaca5f (2018).
54. Buožius, D., Motiejūnas, B., Vaičaitis, V. & Tamulienė, V. Emission of conical THz radiation induced by bichromatic pump X waves in an air plasma. *Phys. Rev. A* **105**, 023521. https://doi.org/10.1103/PhysRevA.105.023521 (2022).
55. Ciddor, P. E. Refractive index of air: new equations for the visible and near infrared. *Appl. Optics* **35**, 1566–1573. https://doi.org/10.1364/AO.35.001566 (1996).
56. Perelomov, A. M., Popov, V. S. & Terent'ev, M. V. Ionization of atoms in alternating electric field. *Sov. Phys. JETP* **23**, 924–934 (1966).
57. Talebpour, A., Yang, J. & Chin, S. Semi-empirical model for the rate of tunnel ionization of N2 and O2 molecule in an intense Ti:sapphire laser pulse. *Opt. Commun.* **163**, 29–32. https://doi.org/10.1016/S0030-4018(99)00113-3 (1999).
58. Wartak, M. S. *Computational Photonics. An Introduction with MATLAB* (Cambridge University Press, 2013).
59. Banerjee, P., Nehmetallah, G. & Chatterjee, M. Numerical modeling of cylindrically symmetric nonlinear self-focusing using an adaptive fast Hankel split-step method. *Opt. Commun.* **249**, 293–300. https://doi.org/10.1016/j.optcom.2004.12.048 (2005).

Acknowledgements
Viktorija Tamulienė is grateful to Luc Bergé for his advice.

Author contributions
V.T.: Concept, simulation, manuscript preparation. V.V.: Concept, supervision of the experiment, manuscript preparation. U.Ž.: Experiment, data analysis, manuscript preparation. All authors reviewed the manuscript.

Funding
This research has been carried out in the framework of the "Universities' Excellence Initiative" programme by the Ministry of Education, Science and Sports of the Republic of Lithuania under the agreement with the Research Council of Lithuania (project No. S-A-UEI-23-6).

Declarations

Competing interests
The authors declare no competing interests.

Additional information
Correspondence and requests for materials should be addressed to V.T.

Reprints and permissions information is available at www.nature.com/reprints.

Publisher's note Springer Nature remains neutral with regard to jurisdictional claims in published maps and institutional affiliations.